Search for ultralight bosons in Cygnus X-1 with Advanced LIGO

Ling Sun[®], ^{1,*} Richard Brito[®], ^{2,†} and Maximiliano Isi[®], ^{3,‡}

¹LIGO Laboratory, California Institute of Technology, Pasadena, California 91125, USA

²Dipartimento di Fisica, "Sapienza" Università di Roma & Sezione INFN Roma1,

Piazzale Aldo Moro 5, 00185 Roma, Italy

³LIGO Laboratory, Massachusetts Institute of Technology, Cambridge, Massachusetts 02139, USA

(Received 25 September 2019; accepted 2 March 2020; published 17 March 2020)

Ultralight scalars, if they exist as theorized, could form clouds around rapidly rotating black holes. Such clouds are expected to emit continuous, quasimonochromatic gravitational waves that could be detected by LIGO and Virgo. Here we present results of a directed search for such signals from the Cygnus X-1 binary, using data from Advanced LIGO's second observing run. We find no evidence of gravitational waves in the 250–750 Hz band. Without incorporating existing measurements of the Cygnus X-1 black hole spin, our results disfavor boson masses in the range $5.8 \le \mu/(10^{-13} \text{ eV}) \le 8.6$, assuming that the black hole was born 5×10^6 years ago with a nearly extremal spin. We then focus on a string axiverse scenario, in which self-interactions enable a cloud for high black-hole spins consistent with measurements for Cygnus X-1. In that model, we constrain the boson masses in the range $9.6 \le \mu/(10^{-13} \text{ eV}) \le 15.5$ for a decay constant $f_a \sim 10^{15}$ GeV. Future applications of our methods to other sources will yield improved constraints.

DOI: 10.1103/PhysRevD.101.063020

I. INTRODUCTION

Ultralight scalar (spin 0) or vector (spin 1) boson particles have been theorized under several frameworks to solve problems in particle physics, high-energy theory and cosmology [1–8]. If such a new fundamental field exists, its occupancy number should superradiantly grow around fast-spinning black holes (BHs). This occurs when $\omega_{\mu}/m < \Omega_{\rm BH}$, where $\omega_{\mu} = \mu/\hbar$ is the characteristic angular frequency of a boson with rest energy μ , m is the boson azimuthal quantum number with respect to the BH's rotation axis, and Ω_{BH} is the angular speed of the outer horizon. The superradiant instability is maximized when the Compton wavelength of the particle is comparable to the characteristic length of the BH, meaning $hc/\mu \sim$ GM/c^2 for BH mass M. If these conditions are satisfied, the number of ultralight bosons around the BH grows exponentially, forming a macroscopic cloud holding up to \sim 10% of the BH mass. This cloud can have a long lifetime, during which it generates continuous, quasimonochromatic gravitational waves (GWs) [9–16].

By detecting such signals, ground-based instruments like Advanced LIGO (aLIGO) [17] and Virgo [18] could probe bosons with masses $\sim 10^{-14}$ – 10^{-11} eV, which are largely inaccessible to other experiments [12,14,15,19]. A search for a stochastic GW background from boson clouds in the

first aLIGO observing run excluded a mass range of $2.0 \le \mu/(10^{-13} \text{ eV}) \le 3.8 \text{ at } 95\% \text{ credibility, under opti-}$ mistic assumptions about BH populations [20]. Methods have been developed to search for continuous GWs from individual clouds, with and without restrictions to specific sky locations [19,21]. Constraints on the boson mass $(\mu \sim 10^{-13} \text{ eV})$ have been suggested using preexisting strain upper limits for continuous GWs obtained from undirected searches [22,23]. Like for the stochastic background, such constraints are contingent on BH populations. Isi et al. [19] modeled the signal waveforms for individual sources with a known sky location, and demonstrated the suitability of a specific search algorithm based on a hidden Markov model (HMM) to efficiently search for such signals [19,24–26]. Two primary types of sources are of interest for such directed searches: remnants from compact binary coalescences (CBCs) [27], and known BHs in x-ray binaries [11,28,29]. Detection prospects for CBC remnants are hurt by their typically large luminosity distances, most likely demanding third-generation detectors [19,30–34]. On the other hand, x-ray binaries have the advantages of being much closer and better localized, hence potentially lying within the sensitive range of existing detectors. Constraints on the mass of axion-like particles have been suggested from spin measurements of BHs in x-ray binaries, roughly disfavoring a range of $6 \times 10^{-13} \le \mu/\text{eV} \le 10^{-11}$ [12,35,36]. For the constraints above, it is implicitly assumed that the boson does not self-interact significantly. This would be the case, e.g., for a quantum chromodynamics axion with decay constant f_a above the grand

lssun@caltech.edu

[†]richard.brito@roma1.infn.it

[‡]maxisi@mit.edu

unification (GUT) scale [37]. However, nonlinear self-interaction could be significant in other proposals, like string axions, if f_a were smaller than the GUT scale [4,11,12,38,39]. Constraints on the boson mass and decay constant can be studied by taking into consideration the nonlinear self-interaction in those scenarios, e.g., the string axiverse.

In this article, we present results from a search for GWs from ultralight scalars in the x-ray binary Cygnus X-1 (Cyg X-1), using data from aLIGO's second observing run (O2) [40,41]. Directed GW searches for sources within x-ray binaries are challenging because of the Doppler modulation induced on the GW by the binary motion. The intrinsic, quasimonochromatic signal is shifted to lower and higher frequencies, resulting in a comb of orbital sidebands when analyzed in the frequency domain. A matched filter is needed to collect the distributed signal power from the sidebands, whose width depends on the intrinsic signal frequency, the BH's projected semimajor axis, and the binary's orbital period. Cyg X-1 is one of the most interesting sources, with or without considering boson self-interactions, because of its relatively high BH mass $(14.8 M_{\odot})$, close proximity to Earth (1.86 kpc), and relatively well measured orbital parameters. In the search, we take advantage of the frequency-domain matched filter of Refs. [24,25] to account for the Doppler modulation.

Unlike for CBC remnants, there is large uncertainty about the age and spin of most BHs in x-ray binaries [42,43]. Moreover, the impact of accretion from the companion is not perfectly understood [12,16]. Boson constraints derived from x-ray binaries, including those presented here, thus require assuming that a cloud would be sufficiently long lasting to be present at the time of observation and that accretion does not substantially affect its formation. When applicable, our constraints factor in the estimated age of Cyg X-1 (4.8–7.6 million years [44,45]) in computing expected strain amplitudes. Another potential issue comes from the spin of the BH in Cyg X-1, which some measurements indicate would be too high (≥ 0.95) to support a boson cloud in the simplest scenarios [44,46,47]. However, there seems to be disagreement in the literature about the BH spin, with some estimates favoring lower values [48–50]. We interpret our results under models with and without the assumption of high spin in Cyg X-1.

In the absence of a detection, we disfavor scalar masses in the range $5.8 \le \mu/(10^{-13} \text{ eV}) \le 8.6$, assuming that the BH has an age of 5×10^6 yr and that it was born with a nearly extremal spin but has an unknown post-superradiance spin. Assuming a high post-superradiance spin, we also consider a specific scenario of the string axiverse [4,11,12,38,39], with a decay constant $f_a \sim 10^{15}$ GeV excluding the mass range $9.6 \le \mu/(10^{-13} \text{ eV}) \le 15.5$. Below, we briefly describe the analysis setup, outline the results and their limitations, and close with future prospects.

II. METHOD AND SETUP

The semicoherent search is based on a HMM tracking scheme combined with a frequency-domain matched filter, Bessel-weighted \mathcal{F} -statistic [19,24,25] (see Appendices A-C) [51]. This efficient search strategy, which achieves the same sensitivity as other stack-slidebased semicoherent algorithms, surmounts some of the computing challenges arising when the orbital parameters are not perfectly measured, and allows for uncertainties in the theoretical prediction of the signal model, e.g., cloud perturbations due to the astrophysical environment. The total observing time $T_{\rm obs}$ is divided into shorter intervals with duration $T_{\rm coh}$, over which the signal power is collected coherently. The segments are labeled by discrete time steps t_k , for $k \in [0, N_T]$ and $N_T = T_{\text{obs}}/T_{\text{coh}} - 1$. Over each interval $[t_k, t_k + T_{coh}]$, the intrinsic GW signal frequency f_0 is assumed to be monochromatic, remaining in one discretized frequency bin of width $\Delta f = 1/(2T_{\rm coh})$. The signal power in each bin is estimated using a matched filter that accounts for Doppler modulation due to the motion of the source within the binary. The central value of bin i is denoted f_i with $i \in [1, N_Q]$, where N_Q is the total number of frequency bins. We adopt the signal model described in Ref. [19] and assume that f_0 can evolve for at most one bin from t_k to t_{k+1} . The HMM is solved by the classic Viterbi algorithm [53], returning the optimal path of signal frequency evolution $f_0^*(t_k)$ for $0 \le k \le N_T$.

Based on the source parameters measured electromagnetically (given in Table I), we search a frequency band of 250–750 Hz. The expected signal strain h_0 would be too weak (\lesssim 8 × 10⁻²⁶) to be detectable below 250 Hz, and the orbital sidebands are too wide (\gtrsim 0.5 Hz) to achieve the desired sensitivity above 750 Hz [19]. Given the source parameters and frequency band, we assume that the first time derivative of the GW frequency is $\dot{f}_0 \sim 10^{-14} - 10^{-13}$ Hz/s [12,19], and hence select $T_{\rm coh} = 10$ d ($\Delta f = 5.8 \times 10^{-7}$ Hz) to cover a \dot{f}_0 range of $0 \leq \dot{f}_0 \leq 6.7 \times 10^{-13}$ Hz/s. Besides this, accretion could result in a small frequency variation due to secular changes in the BH

TABLE I. Cygnus X-1 parameters.

Parameter	Symbol	l Value	Reference
Black hole mass (M_{\odot})	M	14.8 ± 1.0	[54]
Mass ratio	q	1.29 ± 0.15	[55]
Spin	χ	≥ 0.95	[44]
Age (yr)	$t_{\rm age}$	$[4.8, 7.6] \times 10^6$	[44]
Right ascension	α_{\star}	19 ^h 58 ^m 22 ^s	[56]
Declination	δ_{\star}	35°12′0.6″	[56]
Inclination (deg)	ı	27.1 ± 0.8	[54]
Distance (kpc)	d	1.86 ± 0.12	[55]
Orbital period (days)	P	5.599829 ± 0.000016	5 [54]
Projected semimajor axis (l-s)	a_0	$25.56^{+3.15}_{-3.11}$	[54]

parameters. However, since the typical accretion time scale is $t_{\rm acc} \sim 4.5 \times 10^7$ yr at the Eddington rate, the frequency variation due to accretion for Cyg X-1 should be at most $\dot{f_0} \sim -8 \times 10^{-16} (\alpha/0.1)^3 (14.8~M_{\odot}/M) (4.5 \times 10^7~{\rm yr/}t_{\rm acc})$ Hz/s. Because this is, in general, much smaller than the variation due to the cloud dissipation [12,19], we neglect this effect. We search over several values of the light-travel time across the projected semimajor axis of the orbit, in the range $22.45 \le a_0/(1-{\rm s}) \le 28.71$ with bin size 0.05 l-s. This covers the uncertainty implied by the BH mass (M), companion mass, and inclination angle (i) measurements.

The search is parallelized into 1-Hz sub-bands. The detection score S is defined, such that the log likelihood of the optimal Viterbi path equals the mean log likelihood of all paths plus S standard deviations in each sub-band. A detection threshold $S_{\rm th} = 6.22$ for 1% false alarm probability is determined through Monte Carlo simulations, such that searching data sets containing pure noise yields 1% of positive detections with $S > S_{\rm th}$.

III. RESULTS

We analyzed aLIGO O2 data extending from 4 January 2017 to 25 August 2017 UTC (GPS time 1167545066 to 1187733592) [40,41,57]. The search results are recorded in

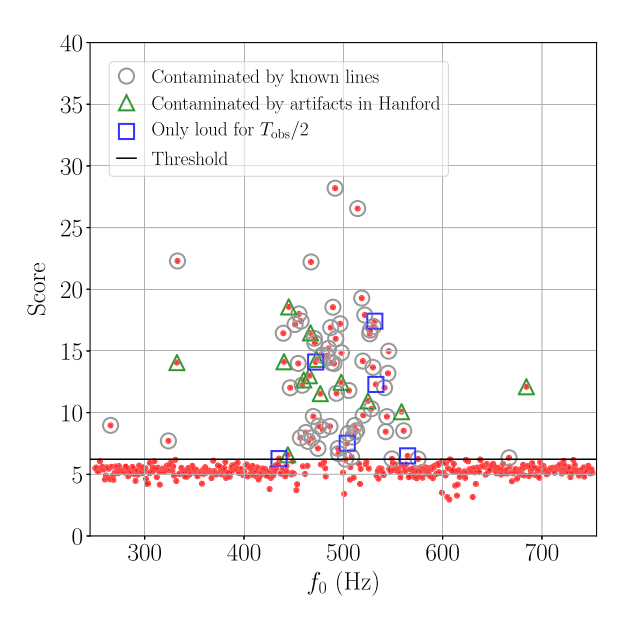


FIG. 1. Detection score S in each 1-Hz sub-band as a function of f_0 . Red dots above the black line (1% false alarm probability threshold $S_{\rm th}=6.22$) are the first-pass candidates. Red dots marked by grey circles are vetoed due to contamination by known instrumental lines. Candidates marked by green triangles are vetoed because their scores are increased when analyzing Hanford only rather than the two detectors combined but below threshold when analyzing Livingston only. Candidates marked by blue squares are vetoed because their scores are increased in one half of $T_{\rm obs}$ but below threshold in the other half. No candidate survives all vetoes.

Fig. 1. Each red dot stands for the detection score S obtained in a 1-Hz sub-band. The black line indicates $S_{\rm th} = 6.22$. We claim a detection if a candidate with $S > S_{\rm th}$ passes a well-defined hierarchy of vetoes and is not identified as originating from an instrumental artifact. We follow up the first-pass candidates found with S > $S_{\rm th}$ (83 in total), finding that none survives a three-stage veto procedure. First, we find that 64 candidates overlap known instrumental lines (grey circles). Second, we eliminate an additional 13 candidates because their significance is higher when analyzing Hanford only rather than the two detectors combined, while doing the same for Livingston yields $S < S_{th}$. This indicates contamination from noise artifacts in Hanford (green triangles). Third, we veto the remaining six candidates because their significance is increased when searching one half of $T_{\rm obs}$, while the other half yields $S < S_{th}$ (blue squares). A full description of the veto procedure can be found in Ref. [25]. The distribution of all the scores obtained in the sub-bands without contamination is shown in Fig. 2.

Unable to claim a detection, we adopt an empirical approach to set a frequentist upper limit on h_0 at 95% confidence ($h_0^{95\%}$). Each black dot in Fig. 3 marks $h_0^{95\%}$ in the corresponding 1-Hz sub-band, derived from the O2 search assuming a source inclination $\iota=27.1^{\circ}\pm0.8^{\circ}$ [54,55]. The procedure for calculating $h_0^{95\%}$ is as follows. First, we perform Monte Carlo simulations by injecting signals with a randomly chosen f_0 within the range 255–256 Hz, but with a fixed h_0 . We draw ι and a_0 uniformly within the ranges 26.3–27.9 deg and 22.45–28.71 1-s, respectively. We repeat this procedure for different h_0 's (step size 1×10^{-26}) until we find the value that yields a 95% detection rate, viz. $h_0^{95\%}=3.9\times10^{-25}$. Next, we calculate $h_0^{95\%}$ over the full

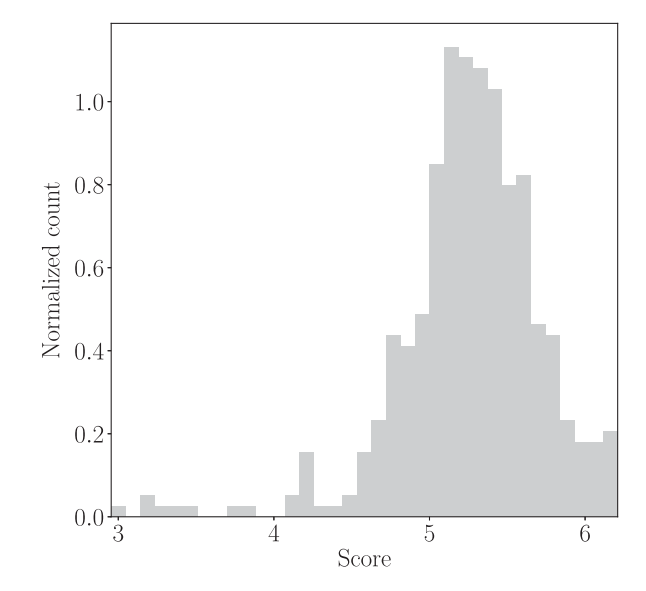


FIG. 2. Distribution of the below-threshold scores from all 1-Hz sub-bands searched. The right edge of the plot indicates the 1% false alarm probability threshold $S_{\rm th}=6.22$.

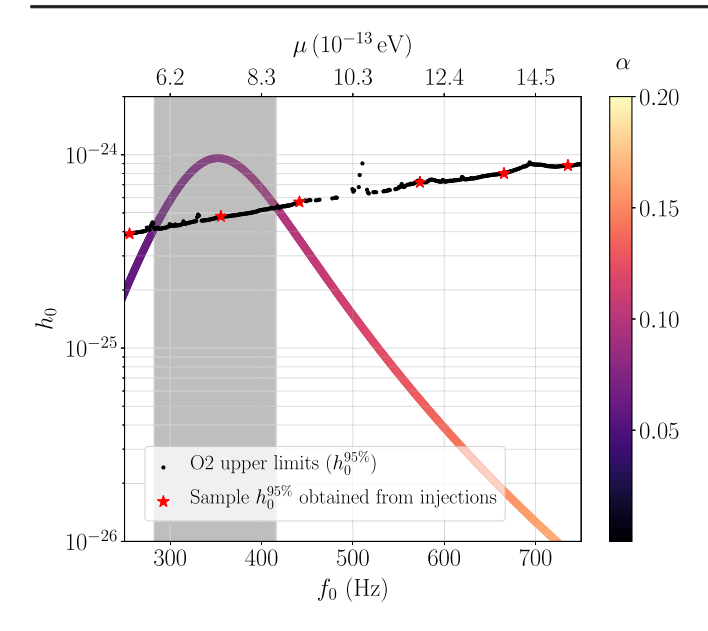


FIG. 3. Frequentist strain upper limits at 95% confidence ($h_0^{95\%}$) and disfavored scalar boson mass range. The colored curve shows the numerically estimated signal strain (h_0) as a function of boson mass (top axis) and GW frequency (bottom axis). The color stands for the fine-structure constant (α). The black dots indicate $h_0^{95\%}$ obtained from the search, assuming the electromagnetically measured orientation $\iota=27.1^\circ\pm0.8^\circ$. The red stars mark $h_0^{95\%}$ obtained through injections in O2 data in six sample 1-Hz subbands. Sub-bands without a marker were vetoed. The shaded region marks the parameter space where $h_0^{95\%}$ beats the analytically estimated strain, and hence corresponds to the disfavored boson mass range $5.8 \le \mu/(10^{-13} \text{ eV}) \le 8.6$ without a detection. The source parameters adopted in the analytic estimation are $M=14.8~M_\odot$, $\chi_i=0.99$, d=1.86~kpc, and $t_{\text{age}}=5\times10^6~\text{yr}$.

frequency band (black dots in Fig. 3) using the analytical scaling $h_0^{95\%}(f) \propto S_h^{1/2}(f)f^{1/4}$ [24,25] [58], where $S_h(f)$ is the aLIGO O2 noise power spectral density [59]. At last, we verify the analytical scaling by repeating the first step in five other 1-Hz bands beginning at 355, 441, 573, 665, and 735 Hz. The resulting $h_0^{95\%}$ values are marked by red stars in Fig. 3. The analytical scaling agrees with the empirical results in the sample sub-bands.

The statistical uncertainty of $h_0^{95\%}$ is less than ~2%, given that the step size of the injected signal strain amplitude is set to 1×10^{-26} . Sub-bands containing a vetoed candidate are contaminated by instrumental artifacts. Hence we cannot place reliable upper limits in these bands (no black dot).

A. Disfavored boson mass

We assume that the scalar cloud is dominated by the energy level l = m = 1, n = 0, where l and n are the orbital azimuthal quantum number and radial quantum number, respectively, and the dominant GW mode is l = m = 2. In Fig. 3, we plot the expected signal amplitude

 h_0 (colored curve) [19] together with the upper-limit $h_0^{95\%}$ (black dots), as a function of expected signal frequency f_0 (bottom axis) and the corresponding boson mass (top axis). To estimate h_0 , we assume $M=14.8~M_{\odot}$, a distance d=1.86 kpc, and an age $t_{\rm age}=5\times10^6$ yr, based on current estimates for Cyg X-1 [44,54,55]. We also assume that the BH had an initial spin $\chi_i=0.99$ before the superradiant cloud growth. The color bar indicates the system's "gravitational fine structure constant," defined as $\alpha=GM\omega_u/c^3$.

The shaded region in Fig. 3, where the upper limits beat the estimated h_0 , highlights the disfavored boson mass range $5.8 \le \mu/(10^{-13} \text{ eV}) \le 8.6$. The estimated h_0 drops significantly for $\mu \gtrsim 7 \times 10^{-13}$ eV ($\alpha \gtrsim 0.08$), because the time scale of the GW signal (τ_{GW}) depends strongly on α [Eq. (23) in Ref. [19]] and h_0 scales as $(1 + t_{\rm age}/\tau_{\rm GW})^{-1}$ [12]. The cloud around an old BH with $t_{\rm age} \sim 5 \times 10^6$ yr, if it ever existed, would have mostly dissipated for $\alpha \gtrsim 0.1$. In Fig. 3, we do not rely on Cyg X-1 spin measurements and rather let the post-superradiance spin of the BH (χ_f) be a free parameter. In the frequency band searched, the conjectured cloud would have spun down the BH such that $\chi_f \lesssim 0.6$ (0.3 $\lesssim \chi_f \lesssim 0.4$ in the shaded region). We do not expect the accreting matter to torque up the BH, since the spin-up time scale is on the order of 10^7 yr (> t_{age}) even at the Eddington accretion rate [44], much longer than the time scale of the superradiant instability (~years). If we refer to existing measurements for Cyg X-1 and assume $\chi_f \ge 0.95$ [44], we obtain $\tau_{\rm GW} \ll$ $t_{\rm age}$ and $f_0 > 1.5$ kHz. The existing method cannot handle the widely spread sidebands (> 1 Hz) at such high frequency. Even if the search could be extended to $f_0 >$ 1.5 kHz with an improved method, the corresponding boson mass ($\mu > 3 \times 10^{-12} \text{ eV}$) cannot be excluded in the absence of a detection, since a signal with $\tau_{\rm GW} \ll t_{\rm age}$ would no longer be present.

The uncertainty in our constraints is dominated by uncertainties in the source properties. The measurement uncertainties of the BH mass, initial spin, and age could lead to an error of at most $\sim 30\%$ on the expected h_0 . The statistical uncertainties of the expected h_0 from numerical modeling and the upper-limit $h_0^{95\%}$ are both on the order of a couple of percent.

B. String axiverse

In the discussion above, we implicitly assume that the boson does not self-interact significantly. Yoshino and Kodama [11] studied the superradiant instability in the string axiverse scenario, taking into consideration the nonlinear self-interaction of string axions. As the scalar field Φ grows through the superradiant instability and reaches a level of $\Phi \sim f_a$, the nonlinear self-interaction triggers a "bosenova," i.e., the axion cloud partially

collapses, with about 5% of the energy falling back into the BH [11,38,39]. After abruptly dropping, the field restarts its superradiant growth until the "bosenova" is triggered again. For bosons that can be probed with aLIGO and Virgo, this process may occur for f_a values smaller than the GUT scale. It was suggested that this periodic process could prevent superradiance from being saturated, allowing the presence of a string-axion cloud around an old, high-spin BH like Cyg X-1.

We may constrain the above scenario by comparing our upper limits $h_0^{95\%}$ to the estimated strain for a cloud that saturates the threshold for the bosenova to occur, namely [11]

$$h_0 \approx 6.2 \times 10^{-25} \left(\frac{f_a}{10^{16} \text{ GeV}}\right)^2 \left(\frac{\mu}{10^{-13} \text{ eV}}\right)^2 \times \left(\frac{M}{14.8 M_{\odot}}\right)^3 \left(\frac{1.86 \text{ kpc}}{d}\right).$$
 (1)

The results are displayed in the (f_a, μ) plane in Fig. 4. The black dots are calculated from $h_0^{95\%}$, and the contours indicate the estimated h_0 values. The boundary between the white and colored regions corresponds to

$$\left(\frac{f_a}{10^{15} \text{ GeV}}\right) = 3.5 \times 10^{-3} \left(\frac{\mu}{10^{-13} \text{ eV}}\right)^{5/2} \left(\frac{M}{14.8 M_{\odot}}\right)^{5/2}, \tag{2}$$

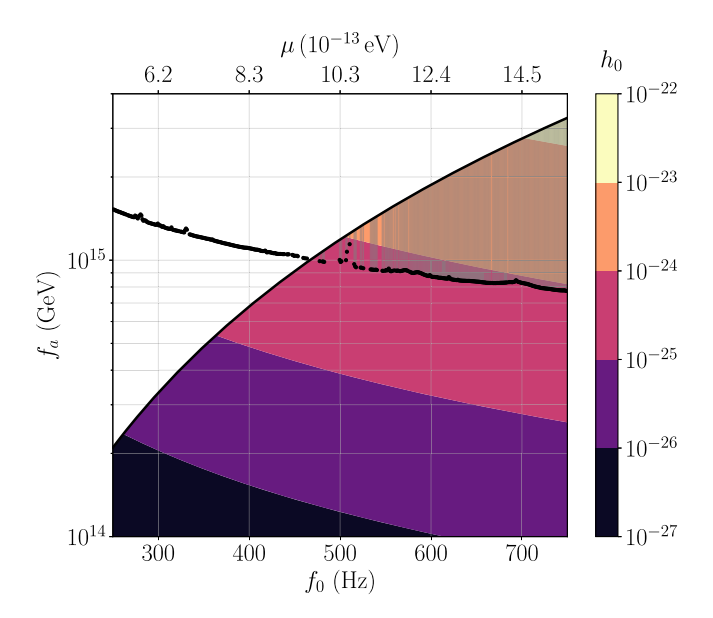


FIG. 4. Excluded parameter space of the decay constant f_a and mass μ of string axions. The black dots indicate the upper limits on f_a as a function of μ (top axis) and f_0 (bottom axis) obtained from the search. The contours indicate the estimated h_0 . The white region is the parameter space where the condition for the bosenova to occur is not satisfied. The shaded region indicates the excluded parameter space.

below which a scalar field grown out of the superradiant instability can reach the level $\Phi/f_a \gtrsim 0.67$ to trigger the bosenova [11,38,39]. Here, we have assumed $\chi_i = 0.99$ and $\chi_f = 0.95$, consistent with the Cyg X-1 observations. We do not derive constraints in the white region, where the condition for the bosenova to occur is not satisfied. The shaded region highlights the (f_a,μ) space excluded by the search. In the mass range $9.6 \le \mu/(10^{-13} \text{ eV}) \le 15.5$, the measurement excludes $f_a \sim 1 \times 10^{15} \text{ GeV}$, an order of magnitude smaller than the GUT scale.

These constraints are contingent on the signal lifetime being longer than $t_{\rm age}$ in this model. Furthermore, this scenario does not take into account the potential impact of radial cloud oscillations: the cloud expands and shrinks during the superradiance and bosenova processes, respectively, potentially modulating the GW frequency on a time scale of minutes [11]. Accurate estimates of signal duration and the frequency modulation will require further numerical study.

IV. CONCLUSION

We reported the results from a directed search for GW signals from a putative scalar boson cloud around the BH in Cyg X-1 in the aLIGO O2 run, using an efficient HMM tracking scheme and a frequency-domain matched filter. We found no evidence of GW signals in the frequency band 250–750 Hz. Assuming an age of 5×10^6 yr, a nearly extremal spin at birth, and an unknown post-superradiance BH spin, our measurement disfavors scalar boson masses in $5.8 \le \mu/(10^{-13} \text{ eV}) \le 8.6$. No reliable constraint can be placed for $\chi_f \ge 0.95$ without considering particle selfinteractions, since the boson field would have disappeared in less than $\sim 10^6$ yr. On the other hand, in the string axiverse scenario, the axion's self-interactions could prevent superradiance from being saturated, enabling the existence of a cloud around an old BH with high spin. We can thus exclude $f_a \sim 1 \times 10^{15}$ GeV for string axions in the mass range $9.6 \le \mu/(10^{-13} \text{ eV}) \le 15.5$. This assumes that $\tau_{\rm GW} > t_{\rm age}$, and that the frequency modulation from the cloud oscillations does not impact the search sensitivity. A more robust analysis will be possible when numerical results of the GW signal time scale and waveform become available under this model. In both scenarios, constraints can only be derived for frequencies where the estimated signal strain exceeds the upper limit obtained from the search. Analyzing a broader frequency band would not have improved the obtained boson mass constraints.

This is a first dedicated GW search for ultralight bosons targeting a known BH. It demonstrates the methodology and interpretation for future similar searches. Besides x-ray binaries, when nearby, well-localized CBCs are detected in upcoming observing runs, the young, isolated remnant BHs will be a target of great interest, free of the complications related to BH age and orbital motion. Future detectors

promise to enable further boson constraints, or even a detection [19,30–34].

ACKNOWLEDGMENTS

We are grateful to Marianne Heida and Riley M. Connors for discussions and suggestions about the source parameters, and the LIGO and Virgo Continuous Wave Working Group for discussions and comments. This search uses LIGO data from the Gravitational Wave Open Science Center (https://www.gw-openscience.org). The authors are grateful for computational resources provided by the LIGO Laboratory. LIGO was constructed by the California Institute of Technology and Massachusetts Institute of Technology with funding from the National Science Foundation, and operates under cooperative agreement PHY-0757058. Advanced LIGO was built under award PHY-0823459. Support for this work was provided by NASA through the NASA Hubble Fellowship Grant No. HST-HF2-51410.001-A awarded by the Space Telescope Science Institute, which is operated by the Association of Universities for Research in Astronomy, Inc., for NASA, under Contract No. NAS5-26555. R. B. acknowledges financial support from the European Union's Horizon 2020 research and innovation programme under the Marie Skłodowska-Curie Grant agreement No. 792862. This work was written in part at the Aspen Center for Physics, which is supported by National Science Foundation Grant No. PHY-1607611. This paper carries LIGO Document No. LIGO-P1900274. M. I. is a NHFP Einstein fellow.

APPENDIX A: HIDDEN MARKOV MODEL

A HMM is a finite state automaton defined by a hidden (unobservable) state variable $q(t_k) \in \{q_1, ..., q_{N_Q}\}$ and an observable state variable $o(t_k) \in \{o_1, ..., o_{N_O}\}$ at discrete times $t_k \in \{t_0, ..., t_{N_T}\}$. The automaton is observed in the state o_j with emission probability [24]

$$L_{o_i q_i} = \Pr[o(t_k) = o_j | q(t_k) = q_i],$$
 (A1)

and jumps between hidden states from t_k to t_{k+1} with transition probability [24]

$$A_{q_iq_i} = \Pr[q(t_{k+1}) = q_i | q(t_k) = q_i].$$
 (A2)

For a memoryless Markov process, the probability that the hidden path $Q = \{q(t_0), ..., q(t_{N_T})\}$ gives rise to the observed sequence $O = \{o(t_0), ..., o(t_{N_T})\}$ is given by [24]

$$Pr(Q|O) = L_{o(t_{N_T})q(t_{N_T})} A_{q(t_{N_T})q(t_{N_{T-1}})} \cdots L_{o(t_1)q(t_1)}$$

$$\times A_{q(t_1)q(t_0)} \Pi_{q(t_0)},$$
(A3)

where

$$\Pi_{q_i} = \Pr[q(t_0) = q_i] \tag{A4}$$

is the prior. The most probable path $Q^*(O)$, maximizing Pr(Q|O), gives the best estimate of $q(t_k)$ over the total observing time.

Discrete hidden states q_i $(1 \le i \le N_Q)$ are mapped one to one to the frequency bins in the output of a frequency-domain estimator G(f) computed over $T_{\rm coh}$, with bin size $\Delta f = 1/(2T_{\rm coh})$. We choose $T_{\rm coh}$ to satisfy

$$\left| \int_{t}^{t+T_{\text{coh}}} dt' \dot{f}_{0}(t') \right| < \Delta f, \tag{A5}$$

for $0 \le t \le (T_{\rm obs} - T_{\rm coh})$, such that searching over \dot{f}_0 is not necessary. For the signal model considered in Ref. [19], Eq. (A1) can be written as

$$L_{o(t_k)f_i} \propto \exp[G(f_i)],$$
 (A6)

where $G(f_i)$ is the log likelihood that the signal frequency f_0 lies in bin $[f_i, f_i + \Delta f]$ during interval $[t_k, t_k + T_{\rm coh}]$. Eq. (A2) takes the simplified form

$$A_{f_{i+1}f_i} = A_{f_if_i} = \frac{1}{2},$$
 (A7)

with all other entries vanishing. The prior is set to $\Pi_{f_i} = N_O^{-1}$ as we have no advance knowledge of f_0 .

APPENDIX B: VITERBI ALGORITHM AND DETECTION SCORE

The Viterbi algorithm is used to compute $Q^*(O)$ recursively [53,60]. At every step k ($1 \le k \le N_T$) forward, the algorithm only keeps N_Q possible state sequences ending in state q_i ($1 \le i \le N_Q$), and stores their maximum probabilities [24]

$$\delta_{q_i}(t_k) = L_{o(t_k)q_i} \max_{1 \le j \le N_O} [A_{q_i q_j} \delta_{q_j}(t_{k-1})],$$
 (B1)

as well as the previous-step states of origin [24],

$$\Phi_{q_i}(t_k) = \arg\max_{1 \le j \le N_O} [A_{q_i q_j} \delta_{q_j}(t_{k-1})], \tag{B2}$$

that maximize the probabilities at step k. The optimal Viterbi path is then reconstructed by backtracking

$$q^*(t_k) = \Phi_{q^*(t_{k+1})}(t_{k+1}), \tag{B3}$$

for
$$N_T - 1 \ge k \ge 0$$
.

In this application, the detection score *S* is defined, such that the log likelihood of the optimal Viterbi path equals the

mean log likelihood of all paths plus S standard deviations, viz. [25]

$$S = \frac{\ln \delta_{f_0^*}(t_{N_T}) - \mu_{\ln \delta}(t_{N_T})}{\sigma_{\ln \delta}(t_{N_T})},$$
 (B4)

with

$$\mu_{\ln \delta}(t_{N_T}) = N_Q^{-1} \sum_{i=1}^{N_Q} \ln \delta_{f_i}(t_{N_T}),$$
 (B5)

and

$$\sigma_{\ln \delta}(t_{N_T})^2 = N_Q^{-1} \sum_{i=1}^{N_Q} [\ln \delta_{f_i}(t_{N_T}) - \mu_{\ln \delta}(t_{N_T})]^2, \quad (B6)$$

where $\delta_{f_i}(t_{N_T})$ denotes the maximum probability of the frequency path ending in bin i ($1 \le i \le N_Q$) at step N_T , and $\delta_{f_A^*}(t_{N_T})$ is the likelihood of the optimal Viterbi path.

APPENDIX C: MATCHED FILTER: BESSEL-WEIGHTED \mathcal{F} -STATISTIC

The optimal frequency-domain matched filter for a continuous-wave signal with no orbital motion is the

maximum-likelihood \mathcal{F} -statistic, $\mathcal{F}(f)$ [61,62], which accounts for the Earth's motion with respect to the Solar System barycenter. When the source orbits a companion, the GW signal frequency is modulated due to the orbital Doppler effect. For a Keplerian circular orbit, the GW strain can be expanded in a Jacobi-Anger series as [24,63]

$$h(t) \propto \sum_{n=-\infty}^{\infty} J_n(2\pi f_0 a_0) \cos[2\pi (f_0 + n/P)t],$$
 (C1)

where $J_n(z)$ is a Bessel function of order n of the first kind. The \mathcal{F} -statistic power is distributed into approximately $M = 2 \operatorname{ceil}(2\pi f_0 a_0) + 1$ orbital sidebands, separated by 1/P, where $\operatorname{ceil}(x)$ denotes the smallest integer greater than or equal to x. Hence we use $G(f) = \mathcal{F}(f) \otimes B(f)$, a Bessel-weighted \mathcal{F} -statistic, in Eq. (A6) for a source in a binary orbit, where B(f) is given by [24]

$$B(f) = \sum_{n=-(M-1)/2}^{(M-1)/2} [J_n(2\pi f a_0)]^2 \delta(f - n/P). \quad (C2)$$

- [1] R. D. Peccei and H. R. Quinn, CP Conservation in the Presence of Pseudoparticles, Phys. Rev. Lett. **38**, 1440 (1977).
- [2] R. D. Peccei and H. R. Quinn, Constraints imposed by *CP* conservation in the presence of pseudoparticles, Phys. Rev. D 16, 1791 (1977).
- [3] S. Weinberg, A New Light Boson?, Phys. Rev. Lett. **40**, 223 (1978).
- [4] A. Arvanitaki, S. Dimopoulos, S. Dubovsky, N. Kaloper, and J. March-Russell, String axiverse, Phys. Rev. D 81, 123530 (2010).
- [5] M. Goodsell, J. Jaeckel, J. Redondo, and A. Ringwald, Naturally light hidden photons in large volume string compactifications, J. High Energy Phys. 11 (2009) 027.
- [6] J. Jaeckel and A. Ringwald, The low-energy frontier of particle physics, Annu. Rev. Nucl. Part. Sci. 60, 405 (2010).
- [7] R. Essig *et al.*, Working Group Report: New light weakly coupled particles, in Proceedings, 2013 Community Summer Study on the Future of U.S. Particle Physics: Snowmass on the Mississippi (CSS2013): Minneapolis, MN, USA, 2013 (2013).
- [8] L. Hui, J. P. Ostriker, S. Tremaine, and E. Witten, Ultralight scalars as cosmological dark matter, Phys. Rev. D 95, 043541 (2017).

- [9] A. Arvanitaki and S. Dubovsky, Exploring the string axiverse with precision black hole physics, Phys. Rev. D 83, 044026 (2011).
- [10] H. Yoshino and H. Kodama, Gravitational radiation from an axion cloud around a black hole: Superradiant phase, Prog. Theor. Exp. Phys. 2014, 43E02 (2014).
- [11] H. Yoshino and H. Kodama, Probing the string axiverse by gravitational waves from Cygnus X-1, Prog. Theor. Exp. Phys. **2015**, 61E01 (2015).
- [12] A. Arvanitaki, M. Baryakhtar, and X. Huang, Discovering the QCD axion with black holes and gravitational waves, Phys. Rev. D 91, 084011 (2015).
- [13] A. Arvanitaki, M. Baryakhtar, S. Dimopoulos, S. Dubovsky, and R. Lasenby, Black hole mergers and the QCD axion at Advanced LIGO, Phys. Rev. D 95, 043001 (2017).
- [14] R. Brito, S. Ghosh, E. Barausse, E. Berti, V. Cardoso, I. Dvorkin, A. Klein, and P. Pani, Stochastic and Resolvable Gravitational Waves from Ultralight Bosons, Phys. Rev. Lett. 119, 131101 (2017).
- [15] R. Brito, S. Ghosh, E. Barausse, E. Berti, V. Cardoso, I. Dvorkin, A. Klein, and P. Pani, Gravitational wave searches for ultralight bosons with LIGO and LISA, Phys. Rev. D 96, 064050 (2017).
- [16] M. Baryakhtar, R. Lasenby, and M. Teo, Black hole superradiance signatures of ultralight vectors, Phys. Rev. D 96, 035019 (2017).

- [17] J. Aasi *et al.* (LSC Collaboration), Advanced LIGO, Classical Quantum Gravity **32**, 074001 (2015).
- [18] F. Acernese *et al.* (Virgo Collaboration), Advanced Virgo: A second-generation interferometric gravitational wave detector, Classical Quantum Gravity **32**, 024001 (2015).
- [19] M. Isi, L. Sun, R. Brito, and A. Melatos, Directed searches for gravitational waves from ultralight bosons, Phys. Rev. D 99, 084042 (2019).
- [20] L. Tsukada, T. Callister, A. Matas, and P. Meyers, First search for a stochastic gravitational-wave background from ultralight bosons, Phys. Rev. D 99, 103015 (2019).
- [21] S. D'Antonio, C. Palomba, P. Astone, S. Frasca, G. Intini, I. La Rosa, P. Leaci, S. Mastrogiovanni, A. Miller, F. Muciaccia, O. J. Piccinni, and A. Singhal, Semicoherent analysis method to search for continuous gravitational waves emitted by ultralight boson clouds around spinning black holes, Phys. Rev. D 98, 103017 (2018).
- [22] V. Dergachev and M. A. Papa, Sensitivity Improvements in the Search for Periodic Gravitational Waves Using o1 LIGO Data, Phys. Rev. Lett. 123, 101101 (2019).
- [23] C. Palomba *et al.*, Direct Constraints on Ultra-Light Boson Mass from Searches for Continuous Gravitational Waves, Phys. Rev. Lett. **123**, 171101 (2019).
- [24] S. Suvorova, L. Sun, A. Melatos, W. Moran, and R.J. Evans, Hidden Markov model tracking of continuous gravitational waves from a neutron star with wandering spin, Phys. Rev. D 93, 123009 (2016).
- [25] B. P. Abbott *et al.*, Search for gravitational waves from Scorpius x-1 in the first advanced LIGO observing run with a hidden Markov model, Phys. Rev. D 95, 122003 (2017).
- [26] L. Sun, A. Melatos, S. Suvorova, W. Moran, and R. J. Evans, Hidden Markov model tracking of continuous gravitational waves from young supernova remnants, Phys. Rev. D **97**, 043013 (2018).
- [27] B. P. Abbott *et al.* (LIGO Scientific and Virgo Collaborations), Gwtc-1: A Gravitational-Wave Transient Catalog of Compact Binary Mergers Observed by LIGO and Virgo During the First and Second Observing Runs, Phys. Rev. X 9, 031040 (2019).
- [28] R. A. Remillard and J. E. McClintock, X-ray properties of black-hole binaries, Annu. Rev. Astron. Astrophys. 44, 49 (2006).
- [29] M. Middleton, Black hole spin: theory and observation, in Astrophysics of Black Holes: From Fundamental Aspects to Latest Developments, Astrophysics and Space Science Library Vol. 440, edited by C. Bambi (Springer, Berlin, Heidelberg, 2016), p. 99.
- [30] S. Ghosh, E. Berti, R. Brito, and M. Richartz, Follow-up signals from superradiant instabilities of black hole merger remnants, Phys. Rev. D **99**, 104030 (2019).
- [31] S. Hild *et al.*, Sensitivity studies for third-generation gravitational wave observatories, Classical Quantum Gravity 28, 094013 (2011).
- [32] B. Sathyaprakash et al., Scientific objectives of Einstein telescope, Classical Quantum Gravity 29, 124013 (2012).
- [33] M. Punturo *et al.*, The Einstein telescope: A third-generation gravitational wave observatory, Classical Quantum Gravity 27, 194002 (2010).

- [34] B. P. Abbott *et al.* (LIGO Scientific Collaboration), Exploring the sensitivity of next generation gravitational wave detectors, Classical Quantum Gravity 34, 044001 (2017).
- [35] V. Cardoso, Ó. J. C. Dias, G. S. Hartnett, M. Middleton, P. Pani, and J. E. Santos, Constraining the mass of dark photons and axion-like particles through black-hole superradiance, J. Cosmol. Astropart. Phys. 03 (2018) 043.
- [36] M. J. Stott and D. J. E. Marsh, Black hole spin constraints on the mass spectrum and number of axionlike fields, Phys. Rev. D 98, 083006 (2018).
- [37] Since the QCD axion mass largely depends on f_a of the Peccei-Quinn symmetry, e.g., $\mu \approx 6 \times 10^{-10} \, \mathrm{eV} (10^{16} \, \mathrm{GeV}/f_a)$ [4], the BHs observable by aLIGO correspond to axions with f_a between the GUT and Planck scales.
- [38] H. Yoshino and H. Kodama, Bosenova collapse of axion cloud around a rotating black hole, Prog. Theor. Exp. Phys. 128, 153 (2012).
- [39] H. Yoshino and H. Kodama, The bosenova and axiverse, Classical Quantum Gravity 32, 214001 (2015).
- [40] LIGO Scientific and Virgo Collaborations, The O2 data release, https://doi.org/10.7935/CA75-FM95 (2019).
- [41] M. Vallisneri, J. Kanner, R. Williams, A. Weinstein, and B. Stephens, The LIGO Open Science Center, J. Phys. Conf. Ser. 610, 012021 (2015).
- [42] C. S. Reynolds, Measuring black hole spin using X-ray reflection spectroscopy, Space Sci. Rev. 183, 277 (2014).
- [43] J. E. McClintock, R. Narayan, and J. F. Steiner, Black hole spin via continuum fitting and the role of spin in powering transient jets, Space Sci. Rev. 183, 295 (2014).
- [44] L. Gou, J. E. McClintock, M. J. Reid, J. A. Orosz, J. F. Steiner, R. Narayan, J. Xiang, R. A. Remillard, K. A. Arnaud, and S. W. Davis, The extreme spin of the black hole in Cygnus x-1, Astrophys. J. **742**, 85 (2011).
- [45] T.-W. Wong, F. Valsecchi, T. Fragos, and V. Kalogera, Understanding compact object formation and Natal Kicks. III. The case of Cygnus x-1, Astrophys. J. **747**, 111 (2012).
- [46] M. Axelsson, R. P. Church, M. B. Davies, A. J. Levan, and F. Ryde, On the origin of black hole spin in high-mass black hole binaries: Cygnus X-1, Mon. Not. R. Astron. Soc. **412**, 2260 (2011).
- [47] D. J. Walton, J. A. Tomsick, K. K. Madsen, V. Grinberg, D. Barret, S. E. Boggs, F. E. Christensen, M. Clavel, W. W. Craig, A. C. Fabian, F. Fuerst, C. J. Hailey, F. A. Harrison, J. M. Miller, M. L. Parker, F. Rahoui, D. Stern, L. Tao, J. Wilms, and W. Zhang, The soft state of Cygnus x-1 observed with nuSTAR: A variable corona and a stable inner disk, Astrophys. J. 826, 87 (2016).
- [48] J. M. Miller, C. S. Reynolds, A. C. Fabian, G. Miniutti, and L. C. Gallo, Stellar-mass black hole spin constraints from disk reflection and continuum modeling, Astrophys. J. 697, 900 (2009).
- [49] T. Kawano, C. Done, S. Yamada, H. Takahashi, M. Axelsson, and Y. Fukazawa, Black hole spin of Cygnus X-1 determined from the softest state ever observed, Publ. Astron. Soc. Jpn. 69, 36 (2017).
- [50] H. Krawczynski, Difficulties of quantitative tests of the kerrhypothesis with x-ray observations of mass accreting black holes, Gen. Relativ. Gravit. **50**, 100 (2018).
- [51] An improved HMM method, which tracks the binary orbital phase and sums the signal power in orbital sidebands

- coherently, proves to be more sensitive [52]. However, the improved method depends on the measurement of the time of passage through the ascending node, which is not available for Cyg X-1. Hence we do not apply the orbital phase tracking in this analysis.
- [52] S. Suvorova, P. Clearwater, A. Melatos, L. Sun, W. Moran, and R. J. Evans, Hidden Markov model tracking of continuous gravitational waves from a binary neutron star with wandering spin. II. Binary orbital phase tracking, Phys. Rev. D 96, 102006 (2017).
- [53] A. Viterbi, Error bounds for convolutional codes and an asymptotically optimum decoding algorithm, IEEE Trans. Inf. Theory 13, 260 (1967).
- [54] J. A. Orosz, J. E. McClintock, J. P. Aufdenberg, R. A. Remillard, M. J. Reid, R. Narayan, and L. Gou, The mass of the black hole in Cygnus X-1, Astrophys. J. 742, 84 (2011).
- [55] J. Casares and P. G. Jonker, Mass measurements of stellar and intermediate-mass black holes, Space Sci. Rev. 183, 223 (2014).
- [56] M. J. Reid, J. E. McClintock, R. Narayan, L. Gou, R. A. Remillard, and J. A. Orosz, The trigonometric parallax of Cygnus X-1, Astrophys. J. 742, 83 (2011).

- [57] The data collected in December 2016 is not used, because there is an end-of-year break starting on 22 December 2016 and the data quality before that (at the beginning of O2) is not optimal.
- [58] Summing the orbital sideband powers incoherently leads to the sensitivity loss scaling as $f^{1/4}$ [24].
- [59] Here the effective $S_h(f)$ is calculated from the harmonic mean of the two detectors over all the 30-min short Fourier transforms collected from GPS time 1180310418 to 1187733592.
- [60] B. G. Quinn and E. J. Hannan, in *The Estimation and Tracking of Frequency* (Cambridge University Press, Cambridge, England, 2001), p. 266.
- [61] P. Jaranowski, A. Królak, and B. F. Schutz, Data analysis of gravitational-wave signals from spinning neutron stars: The signal and its detection, Phys. Rev. D 58, 063001 (1998).
- [62] R. Prix, The F-statistic and its implementation in compute F statistic v2, LIGO Document T0900149, 2019.
- [63] M. Abramowitz and I. A. Stegun, *Handbook of Mathematical Functions: With Formulas, Graphs, and Mathematical Tables* (Courier Corporation, 1965).